Computers and Fluids 266 (2023) 106042

Contents lists available at ScienceDirect

Computers and Fluids

journal homepage: www.elsevier.com/locate/compfluid

# A multi region adjoint-based solver for topology optimization in conjugate heat transfer problems

E. Gallorini [a,*], J. Hèlie [b], F. Piscaglia [a]

[a] Dept. of Aerospace Science and Technology (DAER), Politecnico di Milano, Italy
[b] Vitesco Technologies France SAS, 44 avenue du Gńéral de Croutte, F-31100 Toulouse cedex 1, France

ARTICLE INFO

*Keywords:*
Topology optimization
Adjoint method
Coupled fluid–thermal problems
OpenFOAM
Electronics cooling

ABSTRACT

This work presents an exploration of fluid region optimization within coupled fluid–thermal problems of industrial significance, namely the design of a cooling plate for the thermal management of Printed Circuit Boards (PCB) of electrical propulsion systems. The Topology Optimization technique has been employed through a in-house developed multi-region adjoint solver and a set of customized boundary conditions, allowing the sensitivity computation independently on the problem size. The technique involves the integration of solid material into the computational domain to induce modifications in flow dynamics. This alteration aims to minimize a multi-objective function that considers both the skin temperature and the mechanical power dissipation caused by fluid movement across the domain. The obtained sensitivity values were then employed in optimizing material distribution through the Method of Moving Asymptotes. The derived material distribution was further post-processed to extract the newly optimized configuration of the system. This enabled a thorough evaluation of the optimization methodology's performance and its effectiveness in enhancing the system's overall efficiency.

## 1. Introduction

Conjugate Heat Transfer (CHT) problems have the objective of simulating heat transfer in both solids and fluids simultaneously, encompassing the evolution of pressure, velocity, and temperature. These CHT systems hold significant importance for both academic and industrial research, serving as the standard approach for predicting temperatures in diverse applications such as microchannel-based heat sinks for electronics [1], turbine blades [2], and biological systems [3], among other examples. Interested readers can find additional references in [4]. CHT simulations also play a crucial role in understanding the behavior of cooling systems. In this context, the present study focuses primarily on cooling devices designed for power electronics [5–7]. The widespread utilization of such systems in everyday life underscores the importance of their design phase, which is pivotal for crafting energy-efficient devices and minimizing pollutant emissions. Traditionally, designers have pursued efficiency through resource-intensive and time-consuming trial-and-error approaches based on their expertise. While human knowledge remains an invaluable asset in the design process, a dependable optimization technique can yield rapid and cost-effective initial implementations that outperform the original solutions. The solutions for the solid and fluid regions represent two distinct yet coupled problems, each necessitating distinct tools and strategies. Heat transfer within the solid domain is typically addressed using discrete numerical methods such as Finite Elements (FE) [8], and various optimization approaches have been employed over time. These encompass heuristic algorithms [9] as well as gradient-based methods [10]. In scenarios where the steady-state assumption applies, the resultant Laplace equation admits analytical solutions [7] rooted in Fourier series, which simplifies the problem's intricacies and expedites the optimization process. In the work by [5], the authors employed an analytical technique to ascertain the necessary temperature distribution for optimizing composite substrates. When addressing thermal analysis within the fluid region, it becomes necessary to consider both mass and heat transfer simultaneously. Therefore, if radiation effects are disregarded, as is the case in the remainder of this study, thermal convection must be coupled with diffusion. The Navier–Stokes and energy equations, which describe the fluid's heat and mass transfer, generally lack analytical solutions except for certain simplified configurations. Consequently, achieving fast optimizations as those described for the solid domain is typically impossible. To address this challenge, the equations are tackled using numerical solutions, involving the discretization of the domain into separate elements. Properties defined in such elements or boundary-defining parameters are treated as the design variables for optimization. In complex scenarios, the number

* Corresponding author.
*E-mail address:* emanuele.gallorini@polimi.it (E. Gallorini).

https://doi.org/10.1016/j.compfluid.2023.106042
Received 29 December 2022; Received in revised form 8 August 2023; Accepted 20 August 2023
Available online 23 August 2023

of discrete elements and design variables can quickly escalate, making traditional optimization approaches impractical. The complexity inherent in the design space confines the use of heuristic optimizers like simulated annealing [11] or genetic algorithms [12] to only a few select cases, while gradient-based methods are generally favored due to their faster convergence properties. The primary challenge in gradient-based optimization lies in calculating the gradient. Techniques such as Finite Differences (FD), which rely on the number of design variables, promptly become impractical for intricate applications.

The adjoint method presents an alternative to the approaches mentioned earlier, as it enables users to calculate the gradient of the objective function irrespective of the number of design variables. This can be achieved at a computational cost comparable to that of solving the Navier–Stokes (and potentially energy) equations. The adjoint method finds extensive application across various areas of fluid mechanics, ranging from stability analysis [13] to optimization [14]. In the context of the adjoint methods, two distinct approaches exist [15]: discrete adjoint, where equations are discretized before deriving adjoint equations, and continuous adjoint, where adjoint equations are analytically derived and then discretized within the solution algorithm. In this study, the continuous adjoint method is adopted. This decision is rooted in its flexibility: despite requiring analytical derivation, it results in a fresh set of equations that can be readily implemented into existing codes. In contrast, discrete adjoint optimization entails the utilization of techniques such as Automatic Differentiation [16]. Implementing this within pre-existing software necessitates substantial modifications to the original coding approach, potentially leading to challenges in memory management and an increase in runtime [17]. There are two potential strategies for optimization in fluid dynamics, namely shape optimization (SO) and topology optimization (TO). In SO, the domain's boundaries are modified, whereas in TO, solid material is arranged within the fluid region to alter its configuration.

This manuscript specifically focuses on topology optimization. The history of TO traces back to its origins in structural mechanics optimization [18]. Within this framework, researchers developed interpolation methods like "Solid isotropic material with penalization" (SIMP) [19] and "Rational Approximation of Material Properties" (RAMP) [20]. Additionally, ad-hoc optimization strategies such as the "Method of Moving Asymptotes" (MMA) [21] were devised. In their study [22], the authors introduced TO within fluid dynamics. They focused on optimizing the dissipated power for a Stokes flow under a volume constraint. They included in the momentum balance a penalization term representing the inverse permeability field. This term regulated the distribution of material within the domain, allowing for the retrieval of the Brinkman-type formulation of the Darcy equation for porous media. Subsequent studies extended this formulation to incorporate heat transfer in the fluid. In [23], a multi-objective optimization aimed to minimize both mean temperature and total fluid power dissipation within a system. This was achieved using Finite Element (FE) spatial discretization and the Method of Moving Asymptotes (MMA) for updating design variables. Another approach, presented in [24], combined an FE solver with the Solid Isotropic Material with Penalization (SIMP) method and MMA. Several subsequent papers explored diverse discretization methods, solution approaches, and objective functions [25–27], including mesh modification techniques like Adaptive Mesh Refinement (AMR) [28]. All the aforementioned studies refer to the optimization of the fluid domain with heat transfer as Conjugate Heat Transfer optimization. Anyway, despite the material added as a result of the optimization, which strictly speaking is a liquid with high porosity, no solid simulation is performed. In [29], the authors developed a SO strategy for the conjugate heat transfer problem: clearly, for this approach solid simulation is necessary.

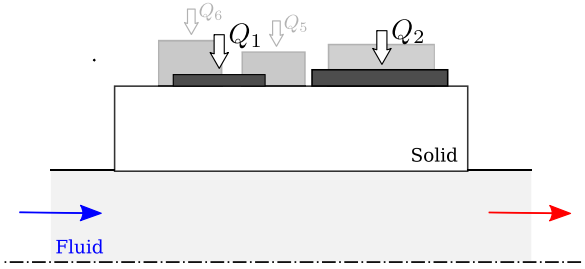


**Fig. 1.** Representation of the computational domain and boundary for a generic CHT problem. In the CFD problem, solid and fluid regions are identified by different (coupled) mesh regions; heat sources are applied at the solid boundary directly.

### 1.1. Motivations of this research

Power electronic components play a crucial role in electric propulsion systems, enabling battery charging, motor control, and power regulation. These components encompass inverters, AC–DC and DC–DC converters, inductors, capacitors, power semiconductors, and transformers. Efficiently managing heat is vital for power electronics to achieve peak performance and prevent component damage. Since power electronics generate heat during operation, effective heat dissipation and temperature control are paramount. Heat sources requiring cooling are situated on the solid boundaries within the channel. These sources apply a consistent heat flux, and their temperature should decrease as a result of optimization efforts. Simultaneously, the dissipation of mechanical power through the cooling channel needs to be regulated due to design limitations within the feeding system. When addressing the optimization of a fluid–thermal problem, researchers often concentrate on the fluid region [27,28], unintentionally ignoring changes in temperature within the solid. Boundary conditions are directly applied to the fluid, potentially yielding misleading outcomes when solid thermal diffusion plays a significant role.

The aim of this study is to explore how topology optimization can generate effective solutions for managing heat in electronic boards within modern electric propulsion systems used in Automotive and Aeronautics. Building on the concept introduced by [29], we apply it to topology optimization (TO) to address multi-region Conjugate Heat Transfer (CHT) problems, where both the solid and the fluid region are simulated to optimize the system.

### 1.2. Paper structure and highlights

The paper is organized as follows: in Section 2, the mathematical formulation of the Conjugate Heat Transfer (CHT) problem is described. Special emphasis is placed on detailing the optimization process within the fluid region and outlining the distinctions, both in terms of equations and boundary conditions, from the conventional approach for this problem type. Section 3 provides an account of the numerical implementation of the novel algorithm. The results are discussed in Section 4, which includes the whole process of designing an optimized cooling plate for electronic circuits, a typical coupled fluid–thermal system of industrial significance. The plate features solid sections where heat fluxes are applied to the boundaries, linking with the fluid regions under optimization. Water serves as coolant, and electronic components are simulated through fixed heat sources applied at the heat sink's boundary. To enhance the behavior of the fluid, information about how temperatures spread is needed. This, in turn, requires to accurately solve the energy equation within the solids and suitable interface boundary conditions to enable information exchange among different mesh regions. Following the optimization process, a seamless distribution of material porosity, varying from no material (0) to the highest feasible value ($\alpha_{max}$), is obtained. This distribution reveals the material's arrangement, but it cannot be directly employed

to manufacture a solid component. Consequently, part of this study is focused on the definition of the boundaries between fluids and solids arising from the optimization. This exploration should enable to gauge how the consideration of solid materials as porous substances influences the projections for optimal solutions. The section introduces a novel, to the best of the authors' knowledge, approach that allows for extracting the optimal geometry and assessing its optimal performance. Finally, Section 5 serves as the concluding discussion of the work. Appendix A validates the implemented boundary conditions for heat sources and fluid–solid interfaces. Appendix B discusses the optimization's convergence to local minima, a behavior expected from a gradient-based approach.

## 2. Mathematical formulation

Conjugate Heat Transfer problems focus on understanding heat transfer between fluid and solid regions. The typical depiction of such a geometry, shown in Fig. 1, illustrates the clear separation between solid and fluid areas at their interface. Within the solid region, heat is primarily transferred through diffusion. This phenomenon is described by the energy equation, which, in this context, corresponds to the heat equation:

$$R^T \equiv -\nabla \cdot D_s \nabla T = 0 \tag{1}$$

being $D_s$ the thermal diffusivity of the solid and $T$ its temperature. In the following, R denotes the residual of the equations.

Within the fluid region, the governing physics is captured by the incompressible Navier–Stokes equations, combined with the energy equation formulated to represent temperature transport and diffusion. This can be expressed as follows:

- mass conservation:

$$R^p \equiv \nabla \cdot \boldsymbol{u} = 0 \tag{2}$$

- momentum balance:

$$\boldsymbol{R}^u \equiv \nabla \cdot (\boldsymbol{u}\boldsymbol{u}) + \nabla p - \nabla \cdot (\nu \nabla \boldsymbol{u}) + \alpha(\eta)\boldsymbol{u} = 0 \tag{3}$$

  where $\boldsymbol{u}$ is the velocity, $p$ the pressure (divided by the density) and $\nu$ the kinematic viscosity. $\alpha(\eta)\boldsymbol{u}$ is a Brinkman penalization term, $\alpha$ is the porosity, which depends on the general design variable $\eta$.
- equation of energy, that for incompressible flows is written in the form of temperature transport-diffusion:

$$R^T \equiv \nabla \cdot (\boldsymbol{u}\, T) - \nabla \cdot (D(\eta)\nabla T) = 0. \tag{4}$$

The inclusion of the penalization term in Eq. (3) serves to facilitate the transition from fluid to solid, which is essential for the process of topology optimization. As $\alpha$ approaches zero, the governing equations for the fluid are reinstated. On the other hand, as $\alpha$ assumes larger values, $\boldsymbol{u}$ tends toward zero, causing temperature transport in the control volume to be primarily governed by solid diffusion. Consequently, Eq. (4) reverts to Eq. (1). The presence of solid material within the fluid domain is thus modulated by $\eta$, through the porosity value $\alpha$. The interface between the fluid and the solid is referred to as the fluid–solid interface. While distinct models characterize the physics of these two regions, it is imperative that at the interface, in the absence of additional heat sources, the fluid's temperature and heat flux align with those of the solid. This fundamental property will be exploited in Section 3 to establish the interface boundary condition for $T$.

The primary objective of this work is to simulate and optimize the heat transfer within a cooling system designed for electronic applications, such as circuit boards. As sketched in Fig. 1, in the context of the current problem, the solid region corresponds to the external case of the cooling system. The sections occupied by heat sources are represented by fixed heat fluxes at the solid boundaries, while the remaining portion of the external domain maintains an ambient temperature. In this application, the optimization primarily targets the fluid region where the coolant circulates, extracting heat from the solid and carrying it away primarily through convection.

### 2.1. Fluid region optimization

Building on the concepts introduced in [28], the optimization problem pertaining to the fluid region is formulated as a constrained optimization. Here, the objective function is denoted as $J$, while the constraints $\boldsymbol{R} = 0$ encompass the steady Navier–Stokes and temperature equations that represent the physical constraints. Notably, the focus on the fluid region underscores that the physical properties of the solid domain remain unaffected by the design variable $\eta$. Anyway, to accurately determine fluid temperature and execute the optimization correctly, it becomes necessary to compute the temperature field within the solid.

In this study, we adopt the Topology Optimization approach. Solid material is introduced into the fluid domain to optimize the objective function $J$. The design variable utilized is the pseudo density $\eta$, assigned to each cell within the optimization domain. Specifically, $\eta = 0$ for the solid, while $\eta = 1$ for the fluid. To interpolate all material properties (including porosity, thermal diffusivity, density, and specific heat) from $\eta$, we employ the Rational Approximation of Material Properties (RAMP), which is formulated as follows:

$$\alpha(\eta) = \alpha_s + (\alpha_f - \alpha_s)\eta \frac{1+q}{\eta+q}, \tag{5}$$

where the subscripts $_s$ and $_f$ indicate properties of the solid and the fluid and $q = 0.1$ for this application. The physical constraints $\boldsymbol{R}$ are enforced using the Lagrange multiplier method, defining an augmented cost function $L$ such that:

$$L = J + \int_V \lambda \cdot \boldsymbol{R}\, dV. \tag{6}$$

Here, $V$ represents the volume of the computational domain, and $\lambda$ denotes the vector of Lagrange multipliers. The nature of the problem involves partitioning the domain into distinct fluid and solid regions, each governed by separate equations and distinct physical constraints. The expression in Eq. (6) can be conveniently reformulated as follows:

$$L = J + \int_{V_f} \lambda \cdot \boldsymbol{R}\, dV + \int_{V_s} \lambda \cdot \boldsymbol{R}\, dV, \tag{7}$$

where $V_f$ and $V_s$ refer to the fluid and solid regions, respectively. The current methodology is based on a gradient-based optimization approach. The gradient of the augmented objective function corresponds to the derivative of $L$ with respect to the vector of design variables $\boldsymbol{\eta}$, often referred to as sensitivity:

$$\frac{\delta L}{\delta \boldsymbol{\eta}} = \frac{\delta J}{\delta \boldsymbol{\eta}} + \frac{\delta}{\delta \boldsymbol{\eta}} \int_{V_f} \lambda \cdot \boldsymbol{R}\, dV + \frac{\delta}{\delta \boldsymbol{\eta}} \int_{V_s} \lambda \cdot \boldsymbol{R}\, dV \tag{8}$$

where the total derivative $\delta\,/\delta\boldsymbol{\eta}$ is used to include contributions from the domain deformation. In the case of fixed boundaries, as for Topology Optimization, (8) reduces to:

$$\frac{\delta L}{\delta \boldsymbol{\eta}} = \frac{\delta J}{\delta \boldsymbol{\eta}} + \int_{V_f} \frac{\partial}{\partial \boldsymbol{\eta}} \lambda \cdot \boldsymbol{R}\, dV + \int_{V_s} \frac{\partial}{\partial \boldsymbol{\eta}} \lambda \cdot \boldsymbol{R}\, dV. \tag{9}$$

To calculate the gradient regardless of the count of design variables, which, in the case of the pseudo-density approach, corresponds to the number of computational elements, the adjoint method is employed. The Lagrange variables $\lambda_f = (q, \boldsymbol{v}, T_a)$ and $\lambda_s = T_a$, which respectively multiply the mass, momentum, and temperature equations, represent the adjoint pressure, velocity, and temperature. In scenarios involving minor perturbations of the variables, Eq. (9) can be reformulated as [28]:

$$\begin{aligned}\frac{\delta L}{\delta \boldsymbol{\eta}} &= \frac{\delta J}{\delta \boldsymbol{\eta}} + \int_{V_f} q \frac{\partial R^p}{\partial \boldsymbol{\eta}}\, dV + \int_{V_f} \boldsymbol{v} \cdot \frac{\partial \boldsymbol{R}^u}{\partial \boldsymbol{\eta}}\, dV + \int_{V_f} T_a \frac{\partial R^T}{\partial \boldsymbol{\eta}}\, dV \\ &\quad + \int_{V_s} T_a \frac{\partial R^T}{\partial \boldsymbol{\eta}}\, dV \\ &= \int_{V_f} R^q \frac{\partial p}{\partial \boldsymbol{\eta}}\, dV + \int_{V_f} \boldsymbol{R}^{\boldsymbol{v}} \cdot \frac{\partial \boldsymbol{u}}{\partial \boldsymbol{\eta}}\, dV + \int_{V_f} R^{T_a} \frac{\partial T}{\partial \boldsymbol{\eta}}\, dV\end{aligned}$$

$$+ \int_{V_s} R^{T_a} \frac{\partial T}{\partial \boldsymbol{\eta}} \, dV + BC_f^p + \\ + \, BC_f^{\boldsymbol{u}} + BC_f^T + BC_s^T + \int_{V_f} \boldsymbol{u} \cdot \boldsymbol{v} \frac{\partial \alpha}{\partial \boldsymbol{\eta}} \, dV + \int_{V_f} \frac{\partial D_f}{\partial \boldsymbol{\eta}} \nabla T_a \cdot \nabla T \, dV \tag{10}$$

being

$$\boldsymbol{R}_f^a = \{ R^q, \boldsymbol{R}^{\boldsymbol{v}}, R^{T_a} \}, \quad R_s^a = R^{T_a} \tag{11}$$

denoted as the adjoint equations, and

$$\boldsymbol{BC}_f^a = \{ BC_f^p, \boldsymbol{BC}_f^{\boldsymbol{u}}, BC_f^T \}, \quad BC_s^a = BC_s^T \tag{12}$$

are integral defined in the domain surface $S$ representing the adjoint boundary conditions. When the adjoint variables are computed to meet the requirements of the adjoint equations $\boldsymbol{R}^a = 0$ and boundary conditions $\boldsymbol{BC}^a = 0$, the sensitivity simplifies to:

$$\frac{\delta L}{\delta \boldsymbol{\eta}} = \int_{V_f} \boldsymbol{u} \cdot \boldsymbol{v} \frac{\partial \alpha}{\partial \boldsymbol{\eta}} \, dV + \int_{V_f} \frac{\partial D_f}{\partial \boldsymbol{\eta}} \nabla T_a \cdot \nabla T \, dV. \tag{13}$$

Eq. (13) is an algebraic relation, making its computation negligible compared to the cost of solving the primal and adjoint equations. These equations are similar and independent of the number of design variables.

### 2.2. Adjoint equations and boundary conditions tailored to CHT problems

The analytical derivation of the adjoint equations and boundary conditions is detailed in [28]. Here, we provide a summary of their formulation and their application to Conjugate Heat Transfer (CHT) problems, omitting the mathematical intricacies covered in the referenced work. The adjoint equations for the fluid domain are as follows:

$$R^q \equiv \nabla \cdot \boldsymbol{v} + \frac{\partial J}{\partial p}\Big|_{V_f} = 0 \tag{14}$$

$$\boldsymbol{R}^{\boldsymbol{v}} \equiv -\nabla \cdot (\boldsymbol{u}\boldsymbol{v}) - (\nabla \boldsymbol{v})\boldsymbol{u} - \nabla \cdot (2\nu\varepsilon(\boldsymbol{v})) + \alpha \boldsymbol{v} + \nabla q - T \nabla T_a + \frac{\partial J}{\partial \boldsymbol{u}}\Big|_{V_f} = 0 \tag{15}$$

$$R^{T_a} \equiv -\nabla \cdot (\boldsymbol{u} T_a) - \nabla \cdot (D_f \nabla T_a) + \frac{\partial J}{\partial T}\Big|_{V_f} = 0. \tag{16}$$

The optimization is focused exclusively on the fluid domain. However, it is essential to determine the evolution of the adjoint variables within the solid. Specifically, a diffusion equation for temperature can be derived:

$$R^{T_a} \equiv -\nabla \cdot (D_s \nabla T_a) + \frac{\partial J}{\partial T}\Big|_{V_s} = 0. \tag{17}$$

The three surface integrals of (10) are used to derive a set of boundary conditions for the adjoint quantities:

$$BC_f^p = \int_{S_f} \left( \boldsymbol{v} \cdot \boldsymbol{n} + \frac{\partial J}{\partial p} \right) \frac{\partial p}{\partial \boldsymbol{\eta}} \, dS = 0 \tag{18}$$

$$BC_f^{\boldsymbol{u}} = \int_{S_f} \left( \boldsymbol{n} \cdot (\boldsymbol{u} \cdot \boldsymbol{v}) + \boldsymbol{v}(\boldsymbol{u} \cdot \boldsymbol{n}) + \nu(\boldsymbol{n} \cdot \nabla)\boldsymbol{v} - q\boldsymbol{n} + \frac{\partial J}{\partial \boldsymbol{u}} + T_a T \boldsymbol{n} \right) \cdot \frac{\partial \boldsymbol{u}}{\partial \boldsymbol{\eta}} \\ \times \, dS - \int_{S_f} \nu(\boldsymbol{n} \cdot \nabla) \frac{\partial \boldsymbol{u}}{\partial \boldsymbol{\eta}} \cdot \boldsymbol{v} \, dS = 0 \tag{19}$$

$$BC_f^T = \int_{S_f} \left( \boldsymbol{n} \cdot \boldsymbol{u} T_a + D_f \boldsymbol{n} \cdot \nabla T_a + \frac{\partial J}{\partial T} \right) \frac{\partial T}{\partial \boldsymbol{\eta}} \, dS - \int_{S_f} T_a D_f \boldsymbol{n} \cdot \nabla \left( \frac{\partial T}{\partial \boldsymbol{\eta}} \right) \\ \times \, dS = 0, \tag{20}$$

similarly, a condition for the adjoint temperature at the solid boundary can be derived:

$$BC_s^T = \int_{S_s} \left( D_s \boldsymbol{n} \cdot \nabla T_a + \frac{\partial J}{\partial T} \right) \frac{\partial T}{\partial \boldsymbol{\eta}} \, dS - \int_{S_s} T_a D_s \boldsymbol{n} \cdot \nabla \left( \frac{\partial T}{\partial \boldsymbol{\eta}} \right) dS = 0. \tag{21}$$

The external boundary consists of various segments, each subject to distinct boundary conditions in the primal problem. Consequently, different adjoint boundary conditions are derived for each of them.

- **Inlet:** velocity $\boldsymbol{u}$ and temperature $T$ are set, so their derivative with respect to $\eta$ is 0. Eqs. (18)–(20) are rearranged to obtain:

$$\boldsymbol{v}_t = 0 \tag{22}$$

$$v_n = -\frac{\partial J}{\partial p} \tag{23}$$

$$(\boldsymbol{n} \cdot \nabla) q = 0 \tag{24}$$

$$T_a = 0. \tag{25}$$

- **Outlet:** at the fluid outlet, Neumann condition applies for both the velocity and the temperature, while the pressure is fixed. As a consequence, the boundary conditions for $q$, for the tangential component of the adjoint velocity $\boldsymbol{v}_t$, and for $T_a$ are:

$$q = \boldsymbol{u} \cdot \boldsymbol{v} + u_n v_n + \nu(\boldsymbol{n} \cdot \nabla) v_n + \frac{\partial J}{\partial u_n} + T_a T \tag{26}$$

$$u_n \boldsymbol{v}_t + \nu(\boldsymbol{n} \cdot \nabla)\boldsymbol{v}_t = -\frac{\partial J}{\partial \boldsymbol{u}_t} \tag{27}$$

$$u_n T_a + D\boldsymbol{n} \cdot \nabla T_a = -\frac{\partial J}{\partial T}. \tag{28}$$

The boundary condition for the normal component of the adjoint velocity $v_n$ is obtained from continuity:

$$(\boldsymbol{n} \cdot \nabla) v_n = \nabla \cdot \boldsymbol{v} - \nabla_{\parallel} \cdot \boldsymbol{v}_t = -\nabla_{\parallel} \cdot \boldsymbol{v}_t \tag{29}$$

being $\nabla_{\parallel}$ the in-plane component of the derivatives at the boundary.

- **Fixed-temperature wall:** when the temperature remains constant at the wall, deriving the boundary condition for $T_a$ yields:

$$T_a = 0 \tag{30}$$

valid for walls of both solid and fluid domains. Boundary conditions for the adjoint pressure and velocity are as in Eqs. (22)–(24).

- **Fixed heat flux wall:** the heat flux remains constant where the heat sources are located within the solid domain, leading to the following conditions:

$$\kappa_s \boldsymbol{n} \cdot \nabla T = q. \tag{31}$$

being $\kappa_s$ the thermal conductivity of the solid. The adjoint pressure and velocity remain unspecified, while for the adjoint temperature, the following relationship applies:

$$D_s \boldsymbol{n} \cdot \nabla T_a = -\frac{\partial J}{\partial T}. \tag{32}$$

- **Fluid–solid interface:** at the fluid–solid interface the following relations for the temperature hold:

$$T_s = T_f \tag{33}$$

$$\kappa_s \boldsymbol{n} \cdot \nabla T_s = \kappa_f \boldsymbol{n} \cdot \nabla T_f. \tag{34}$$

Similarly, for the adjoint temperature:

$$T_{a,s} = T_{a,f} \tag{35}$$

$$\kappa_s \boldsymbol{n} \cdot \nabla T_{a,s} = \kappa_f \boldsymbol{n} \cdot \nabla T_{a,f}. \tag{36}$$

Calculating the temperature and adjoint temperature within the solid domain is crucial. Even though the optimization focuses solely on the fluid, the heat sources are located at the solid boundary. Consequently, the heat flux and, as discussed earlier regarding the adjoint boundary conditions for the fixed heat flux wall, the "adjoint heat flux" are established at these specific locations. This is distinct from the rest of the boundary, where the temperature is set to the ambient value. As a result, temperature perturbations diffuse within the solid and are transmitted to the fluid through the interface, altering the sensitivity field and influencing the optimization outcome.

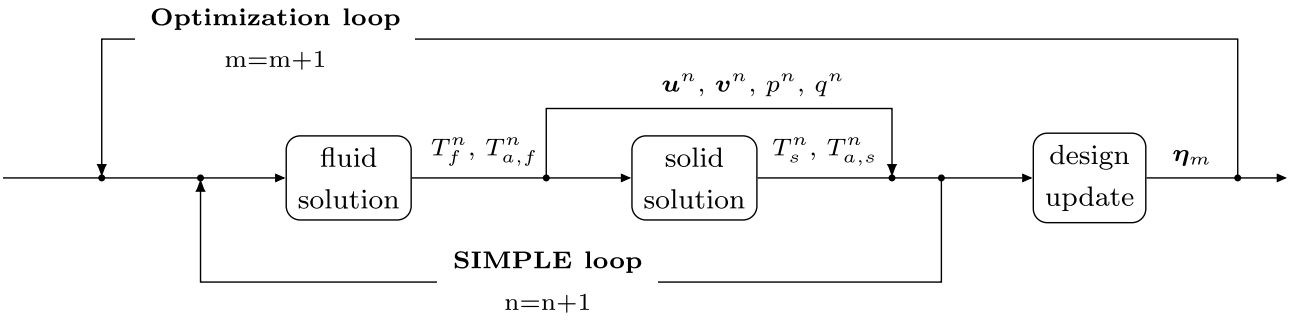


**Fig. 2.** Schematics of the solution algorithm for the optimization problem.

### 2.3. Multi-objective optimization of CHT problems

Considering the insights from the preceding sections, the optimization problem can be reformulated in relation to the augmented objective function $L$ as follows:

$$\text{minimize } L(p, \boldsymbol{u}, T, \eta). \tag{37}$$

The initial objective function $J$ is encompassed within $L$ (Eq. (6)). Typically, CHT problems require the optimization of two functions, one related to mechanics and the other to thermodynamics. For this reason, also in the presented method there are two distinct objective functions: $J_1$, reflecting the mechanical power dissipated by the fluid through the boundaries:

$$J_1 = -\int_{S_1} (p + \frac{1}{2}\boldsymbol{u}^2)\boldsymbol{u} \cdot n \, dS, \tag{38}$$

and $J_2$, representing the difference between the heat sources temperature and the ambient one $T_{amb}$

$$J_2 = \int_{S_2} \frac{1}{2}(T - T_{amb})^2 \, dS. \tag{39}$$

$S_1$ and $S_2$ in Eqs. (38)–(39) correspond to the surfaces where $J_1$ and $J_2$ are defined, specifically the inlet and outlet for the former, and the heat sources for the latter. These function objects carry practical significance. The cooling system relies on a pump that supplies mechanical power, which must match the required amount. Smaller pumps can provide reduced power, leading to decreased weight, costs, and energy consumption. Additionally, heat flux is typically generated by printed circuit boards, which can suffer damage or performance degradation if their temperature surpasses a certain threshold. Hence, the need to regulate the temperature of the heat sources. Consequently, the overall objective function becomes a linear combination of $J_1$ and $J_2$:

$$J = w_1 J_1 + w_2 J_2 \tag{40}$$

where $w_1$ and $w_2$ represent weights determined through a trial and error process, influenced by the relative significance of mechanical and thermal optimization. $J_1$ and $J_2$ are defined at the boundaries but are zero within the internal domain, which results in the corresponding terms in Eqs. (14)–(17) also being zero. As explained in the preceding section, physical constraints are enforced by employing Lagrange multipliers and the sensitivity is computed by satisfying the adjoint equations and their associated boundary conditions. Typically, other constraints are applicable. For this specific problem, we set a condition that limits the maximum amount of solid introduced by the topology optimization to a fraction of the total fluid volume:

$$\sum_{j=1}^{n_c} (1 - \eta_j) \, dV_j - \Phi_{max} V_f < 0 \tag{41}$$

where $n_c$ is the total number of Control Volumes (CVs) in the fluid domain and $\Phi_{max}$ is the maximum volume fraction that can be solid.

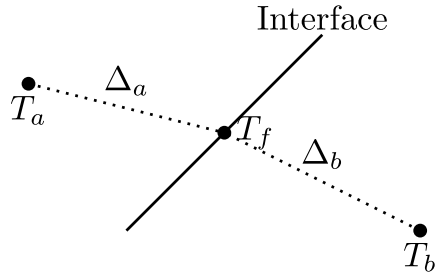


**Fig. 3.** Representation of a generic interface for $T$.

## 3. Numerical implementation

The solver for the optimization problem, as depicted in Fig. 2, is implemented through a set of in-house dynamic C++ libraries developed within the open-source Computational Fluid Dynamics (CFD) code OpenFOAM [30,31]. The spatial discretization follows the Finite Volume (FV) method. For further insights into the numerical approach, one can refer to [28]. Here, we highlight the key steps of the optimization process and outline the necessary modifications to address multi-region Conjugate Heat Transfer (CHT) problems. In the fluid region, the computation of $p$, $\boldsymbol{u}$, and $T$ involves solving the steady incompressible Navier–Stokes and temperature equations (Eqs. (2)–(4)). The pressure–velocity coupling is managed using the Semi-Implicit Method for Pressure Linked Equations (SIMPLE) algorithm [32]. This approach facilitates the determination of $p$ and $\boldsymbol{u}$ across the entire computational domain. Subsequently, the velocity values are utilized to solve the temperature equation. Upon obtaining the primal values, the adjoint equations (Eqs. (14)–(16)) are solvable. Notably, the adjoint temperature equation is decoupled from the others and is solved first. The structure of the adjoint pressure–velocity closely mirrors their primal counterparts, and the same SIMPLE algorithm ensures coupling of pressure and velocity. Typically, at this stage of the simulation, either the $n$th iteration of the SIMPLE loop concludes upon reaching convergence criteria, or the loop starts again from the beginning. In the context of CHT problems, this changes because the equations for the solid domain are solved as part of the SIMPLE iteration. Temperature and adjoint temperature within the solid domain (Eqs. (1) and (17)) are solved using the same tools employed for the fluid. The temperature equation is resolved first, followed by its adjoint counterpart once the adjoint boundary conditions are updated.

Subsequently, the implementation of the interface boundary condition for $T$ is discussed. This framework applies similarly to $T_a$, where the physics are modeled by analogous equations. At the fluid–solid interface, certain conditions hold as long as no additional heat flux is specified along this section of the boundary:

$$\begin{cases} T_f|_a = T_f|_b \equiv T_f \\ \kappa_a \nabla T_a = \kappa_b \nabla T_b. \end{cases} \tag{42}$$

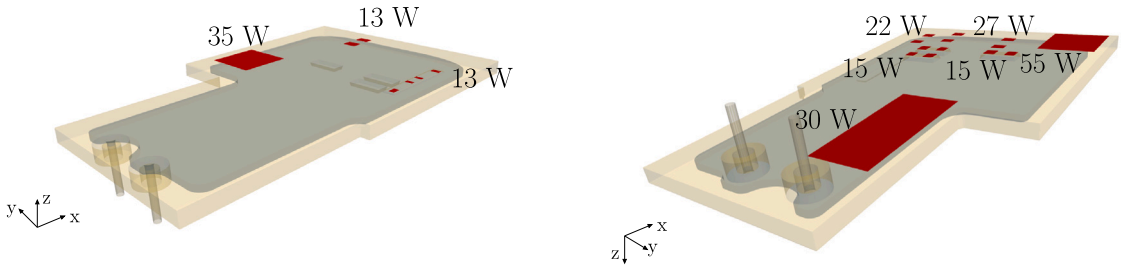


**Fig. 4.** Geometry used for CHT optimization: The solid region is highlighted in yellow, while the fluid region is depicted in blue. Within the illustration, the heat sources are denoted in red, indicating their respective provided thermal power for the upper (left) and lower (right) walls.

The discrete form of the condition (42) is rewritten as:

$$\kappa_a \frac{T_a - T_f}{\Delta_a} = -\kappa_b \frac{T_b - T_f}{\Delta_b}. \tag{43}$$

where $\Delta_a$ and $\Delta_b$ represent the cell center-face distance as represented in Fig. 3. As a consequence:

$$T_f = \frac{T_b \kappa_b \Delta_a + T_a \kappa_a \Delta_b}{\kappa_b \Delta_a + \kappa_a \Delta_b}. \tag{44}$$

This calculated $T_f$ is then employed to compute face-fluxes for balance equations, discretized using the Finite Volume method. Upon determining $T$ and $T_a$, the $n$th iteration of the SIMPLE loops concludes, as depicted in Fig. 2. The discretization of the face fluxes in Eqs. (43)–(44) is a first-order approximation. This implementation has been substantiated in the literature to yield sufficiently accurate solutions for the specific problem at hand [33], as validated in Appendix A. Notably, more accurate alternatives exist [34,35], yet their discussion fall beyond the scope of the current work. Both the primal and adjoint variables are essential for computing sensitivity in the constrained problem (Eq. (13)) and updating the design. Sensitivity guides the gradient-based optimization approach toward optimal values, and the Method of Moving Asymptotes (MMA), introduced in [21], employs this information to update the design variable. MMA, originally designed for structural mechanics topology optimization, can be readily adapted for the current problem. The optimization is an iterative process, generating and solving strictly convex subproblems that approximate the original one. Upon updating the design variable, its value is used to compute material properties through the RAMP (see Section 2.1). The $m$th iteration of the optimization cycle concludes, and the objective function is computed. If convergence criteria are met, the simulation halts; otherwise, the optimization step is repeated.

## 4. Results

### 4.1. Multi objective optimization

The presented CHT optimization has been implemented within a cooling system designed for refrigerating electronic devices. The geometry, depicted in Fig. 4, comprises an external box representing the solid domain and a fluid coolant. The solid section is composed of die-casted aluminum, while the fluid component is water. An inlet volumetric flow rate of 8 L/min is imposed, where the fluid temperature matches the ambient temperature: $T_{in} = T_{amb} = 338$ K. The system involves 21 heat sources generating a total thermal power of 440 W. These heat sources possess varying dimensions and power levels, situated on sections of the upper and lower external metallic casing. Details regarding their positions and provided power are summarized in Fig. 4.

The remaining portions of the external boundary are maintained at $T = T_{amb}$. The conditions for the fluid–solid interface are discussed in Section 3. For the solid and fluid domains, two separate computational grids have been generated, aiming to achieve a balance between solution accuracy and computational efficiency. Due to the iterative nature of optimization, the simulations are repeated throughout the loop (Fig. 2), potentially incurring substantial computational costs. Consequently, careful design of the domain dimensions is essential. The selected mesh comprises $1 \cdot 10^6$ elements for the solid region and $1.8 \cdot 10^6$ for the fluid region. Turbulence modeling employs the $\kappa - \omega$SST model with wall functions, while the frozen hypothesis is adopted to eliminate the need for additional equations concerning adjoint turbulence. Optimization simulations are conducted using fully converged results, requiring the SIMPLE outer loop to be repeated for 5000 iterations. Sensitivity calculations are subsequently performed, with outcomes passed to the MMA algorithm to update the inverse permeability field. Choosing appropriate weights $w_1$ and $w_2$ for the multi-objective function in Eq. (40) is a complex task. Different weight combinations yield distinct optimal values for $J_1$ and $J_2$, resulting in diverse solid material distributions. The final configuration choice depends on user preferences; however, given the problem's intricacies, anticipating a solution beforehand is challenging. To address this, multiple optimizations employing varying weight combinations are executed, and a selection of results is presented here. An observation of Eq. (15) reveals the presence of $-T\nabla T_a$ in the adjoint momentum equation. Owing to the solution algorithm's segregated structure, this term is explicitly computed from known $T$ and $T_a$ values, contributing to the linear system's right-hand side. In regions characterized by high temperatures and abrupt adjoint temperature fluctuations, this term can attain exceptionally large values. Consequently, it influences $\upsilon$ and, consequently, the optimal material distribution, leading to a fragmented and noisy solution. An effective approach to mitigate this effect involves solving an equation for the normalized temperature $\tilde{T} = (T - T_{amb})/T_{amb}$. The original temperature $T$ can be obtained from $\tilde{T}$ through simple scaling, preserving the primal problem's physics. Simultaneously, the impact of $-T\nabla T_a$ in the adjoint momentum equation diminishes, resulting in a smoother optimal material distribution. This approach offers an added advantage: the solution is independent of the cooling fluid's temperature, aside from physical properties. Hence, the optimization weights could serve as a reasonable starting point for optimizations under varying thermal conditions. An initial reference simulation has been executed to outline the characteristics of the non-optimized solution. Fig. 5 illustrates the temperature distribution in the upper and lower walls, alongside velocity streamlines color-coded by velocity magnitude. Regions of critical temperature are primarily located at the bottom. Notably, heat sources of 22 and 27 W, as well as the 55 W source, induce an approximate 10 K temperature rise.

Conversely, sets of 13 W (top wall) and 15 W (bottom wall) heat sources cause modest temperature fluctuations due to their positioning on the top of spreaders. Given the inlet's orientation perpendicular to the top, water impinges on the wall, leading to redirection toward the channel. This design prevents the flow from reaching the heat sources and instead prompts a U-turn in the frontal region. The study's initial parameter evaluation focuses on the impact of the thermal objective function weight on the optimization outcome. Four distinct cases are presented, where $w_1$ remains fixed at $w_1 = 1 \cdot 10^2$, while $w_2$ varies, as outlined in Fig. 6, ranging from 0 (indicating negligible influence of the thermal contribution) to $10^{10}$, effectively prioritizing $J_2$ within the optimization process.

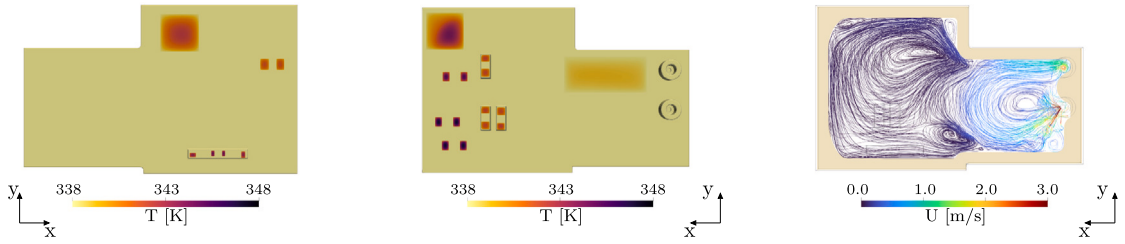


**Fig. 5.** Results from the reference simulation: the temperature profile of the upper wall is presented on the left, followed by the temperature profile of the lower wall in the center. On the right, velocity streamlines are displayed, color-coded to represent velocity magnitude.

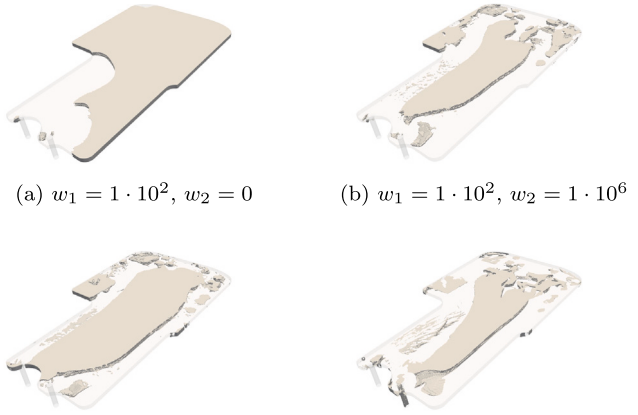

(a) $w_1 = 1 \cdot 10^2$, $w_2 = 0$ (b) $w_1 = 1 \cdot 10^2$, $w_2 = 1 \cdot 10^6$

(c) $w_1 = 1 \cdot 10^2$, $w_2 = 1 \cdot 10^7$ (d) $w_1 = 1 \cdot 10^2$, $w_2 = 1 \cdot 10^{10}$

**Fig. 6.** Results of the optimization: solid material distribution obtained imposing a threshold of $\eta = 1 \cdot 10^{-5}$ to the pseudo density field at different values of $w_2$ for $w_1 = 1 \cdot 10^2$.

The optimized material distributions, depicted in Fig. 6, have been obtained by identifying regions where $\eta < 1 \cdot 10^{-5}$ and illustrate how the non-trivial impact of $w_2$ manifests in the results. Each optimization cycle has been repeated 40 times, except for case *b*, which required 80 repetitions to attain objective function convergence. In the case denoted as *a* in Fig. 6, the optimization results in a solid configuration that facilitates the fluid's direct flow from the inlet to the outlet, effectively reducing dissipated mechanical power as anticipated. Incorporating a thermal objective function leads to the placement of porous material at the cooling system's center, diverting the flow from its non-optimized path to favor enhanced heat exchange. Conversely, cases *b*, *c*, and *d* compel the flow, through solid placement, to access the rear region of the cooler, where the majority of thermal power is supplied. Notably, case *c* showcases a solid septum preventing direct flow exchange from the inlet to the outlet before passing through the rear duct section.

For cases *b*, and *d* the solid does not localize in the front region, leaving the possibility for direct mass exchange between the inlet and outlet. This apparent similarity between two results with very different values in terms of $w_2$ hides instead a clear difference in the flow behavior as represented in Fig. 7. For the case *b*, the flow hits the solid and splits so that part of it reaches the heated region and part of it reaches directly the outlet reducing the pressure losses. For the case *d* the way is opposite, and a minor part of the flow, the one that has not been completely heated up, is redirected from the rear regions to the inlet due to the shape of the solid. In that way, the pressure losses are increased together with the flow rate that reaches the heat sources, promoting the extraction of thermal power.

The optimized geometries' performances are summarized by the histograms in Fig. 8, showing the normalized difference between the optimal value of the *i*th objective function, $J_{i,OPT}$, and the non-optimized value, $J_{i,REF}$, calculated as:

$$\Delta J_i = \frac{J_{i,OPT} - J_{i,REF}}{J_{i,REF}} \cdot 100 \tag{45}$$

Of note, cases *a* and *b* exhibit a 12% reduction in dissipated mechanical power; however, case *b* achieves a higher skin temperature reduction (71% versus 53% in case *a*). While cases *c* and *d* yield slightly greater $J_2$ reductions compared to case *b*, i.e., 73% and 76% respectively, these improvements are accompanied by increased dissipated mechanical power (+3% and +500%). Furthermore, case *d* demonstrates a substantial increase in $J_1$, a departure from cases *b* and *c*, despite their similar geometric setups. This anomaly, as discussed in the next section, stems from the solid stack at the inlet channel: the weight of $J_1$ is so low that its influence is not sufficient to remove it, decreasing the mechanical performance.

### 4.2. Post-processing of the optimal result

Topology optimization for industrial problems should lead to the creation of feasible components. However, the optimal solutions from Section 4.1 cannot be directly used as they are and require post-processing because: (a) the outcome of multi-objective optimization is a set of ideal solutions, leaving the final decision to the user to select one or a group that meets the requirements; (b) the solution involves a porous material arrangement with interpolated physical properties (as detailed in Section 2). Consequently, the optimization outcome provides an indication of achievable performance, which should be validated by substituting the porous material with solid material. For post-processing and performance assessment, we have selected cases *c* and *d* from Fig. 6.

As discussed in Section 4.1, optimization significantly impacts simulation results, altering flow paths and heat exchange between the solid and fluid. In both cases, a major portion of the solid accumulates in the central domain. Consequently, the flow is directed toward the system's rear, where heat sources are positioned. This configuration mirrors curved arrangements typical of cooling systems and heat exchangers [36]. Despite increased pressure drop and power requirements, this design enables the flow to traverse regions with higher temperatures, extracting thermal power and reducing heat source skin temperatures. The solid structure consists of a broad central component and smaller elements spread across the remaining domain. The central component notably influences flow path modifications, narrowing the duct's cross-section and accelerating the fluid toward the rear. The smaller elements focus on enhancing heat exchange, with a secondary impact on the overall flow path; their role will be further investigated in the following. The process of extracting the solid region involves various steps, manipulating the $\eta$ field using the `pyvista` library [37].

Initially, a threshold value $\eta_{th}$ is selected, distinguishing fluid from solid regions. In this work, a suitable threshold is $\eta_{th} = 1 \cdot 10^{-5}$. The solid regions resulting from threshold clipping are then divided into separate components. However, certain connected solid parts are too small and have minimal influence on simulation results. These

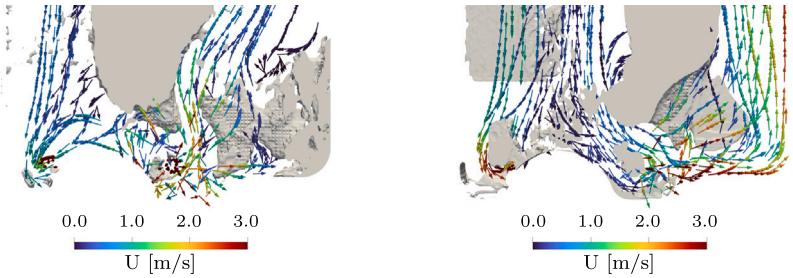


**Fig. 7.** Flow path at the front of the cooling duct: for the case $b$ (left) of Fig. 6 the flow goes from the inlet through the outlet, vice versa for the case $d$ (right).

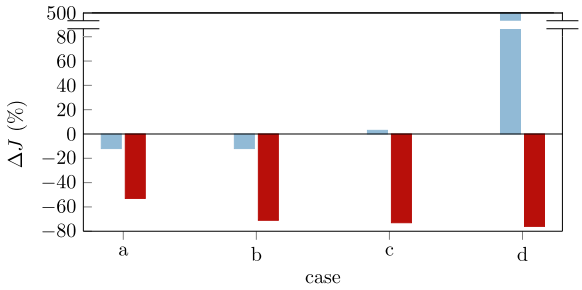


**Fig. 8.** Variation of the objective functions compared to the non-optimized case computed as $\Delta J$ (Eq. (45)). $\Delta J_1$ (■) and $\Delta J_2$ (■) are represented for the cases of Fig. 6.

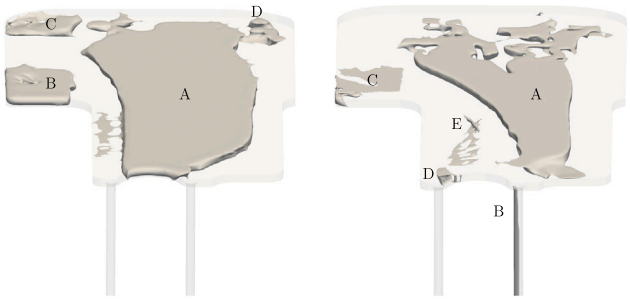


**Fig. 9.** The post-processing analysis involves extracting solid surfaces from cases $c$ (left) and $d$ (right) of Fig. 6. The diverse, unconnected components, denoted by capital letters, have been identified, separated, and can independently integrated into the ultimate geometry.

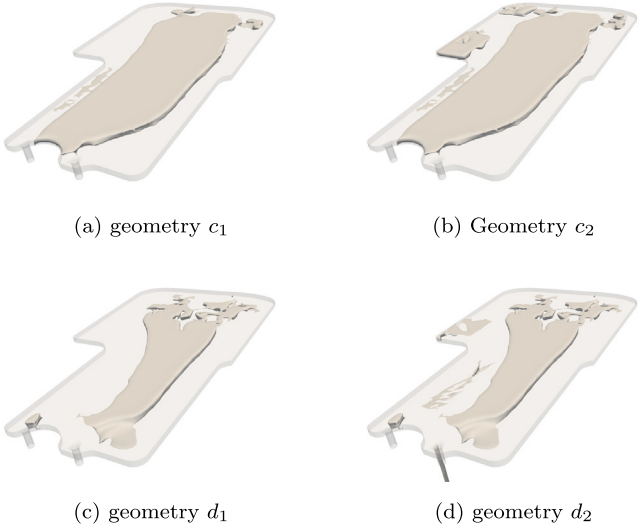


**Fig. 10.** The geometries obtained by considering distinct unconnected elements, as identified in Fig. 9, resulting from the post-processing of cases $c$ and $d$ depicted in Fig. 6.

components are omitted to reduce overall computational time. The selection depends on the relative solid structure volume compared to the largest one, and this choice should be adjusted case by case. At this stage, the solid structures exhibit jagged surfaces with sharp edges that are challenging to replicate in real applications and may cause meshing and simulation issues. To mitigate this, the results are smoothed using the non-shrinking Taubin filter [38]. Once the $\eta$ field has been post-processed, the new solid surfaces can be extracted and used to modify the original geometry. The procedure just described has been applied to cases $c$ and $d$ of Fig. 6 and the results are represented in Fig. 9: several elements are extracted from the original porosity distribution and used to identify the new fluid–solid interface. Since elements are unconnected, they are included separately during the meshing process, and, including or excluding some of them, the different geometries of Fig. 10 are obtained. With such an approach it is easy to separate the different components and study their influence on the objective function. For the case $c$, two geometries have been created: the first one, denoted as $c_1$, includes the main element only, indicated with A in Fig. 9. In the second, $c_2$, components B, C, and D are included together with A. Similarly, for the case $d$, elements of Fig. 9 are assembled in two different geometries. Case $d_1$ includes just the elements A and D, $d_2$ also B, C, and E.

Fig. 11 illustrates the temperature distribution and velocity streamlines for four configurations: $c_1$, $c_2$, $d_1$, and $d_2$. In all cases, there is a decrease in skin temperature compared to Fig. 5, which is more pronounced for elements located outside the spreaders. The temperature variation is comparable for couples $c_1 - c_2$ and $d_1 - d_2$, with the former resulting in a greater reduction than the latter.

In Fig. 12, vertical temperature profiles are presented at three distinct locations: the centers of heat sources with power outputs of 35 W, 55 W, and 22 W. The top panel clearly demonstrates the impact of adding elements B and C to cases $c_2$ and $d_2$, respectively, which notably reduces the temperature peak. This effect is particularly evident in case $c_2$, where the absence of temperature discontinuities indicates the presence of only solid material. Similarly, element C contributes to lowering the temperature of $c_2$ compared to $c_1$, although to a lesser extent in this case. For the 22 W heat source, both configurations $c$ and $d$ maintain identical geometry and temperature distributions. Fig. 11 also reveals a noticeable deviation in the flow path compared to Fig. 5. The optimized flow path now follows the new boundaries and converges toward the rear of the channel. Notably, in configurations $c_1 - c_2$, the solid region is wider than in $d_1 - d_2$, leading to a reduction in the channel section and higher velocities for the former geometries. Quantitative analysis complements the qualitative discussion presented in Fig. 11. The variation of the objective functions $J_1$ and $J_2$ (Eq. (45)) has been computed and is graphically represented in Fig. 13. The behavior of objectives differs for cases $c_1$ and $c_2$: $J_1$ slightly decreases by 10% for $c_1$, but increases by 52% for $c_2$. Meanwhile, $J_2$ decreases by around 50% for both cases (49% and 56% respectively). The $\Delta J_2$ is similar to that obtained for the porous solution, but the dissipated mechanical power is higher when considering all components. This outcome is expected since the porosity models the fluid-to-solid transition. However, the approximation of viscous effects at fluid–solid

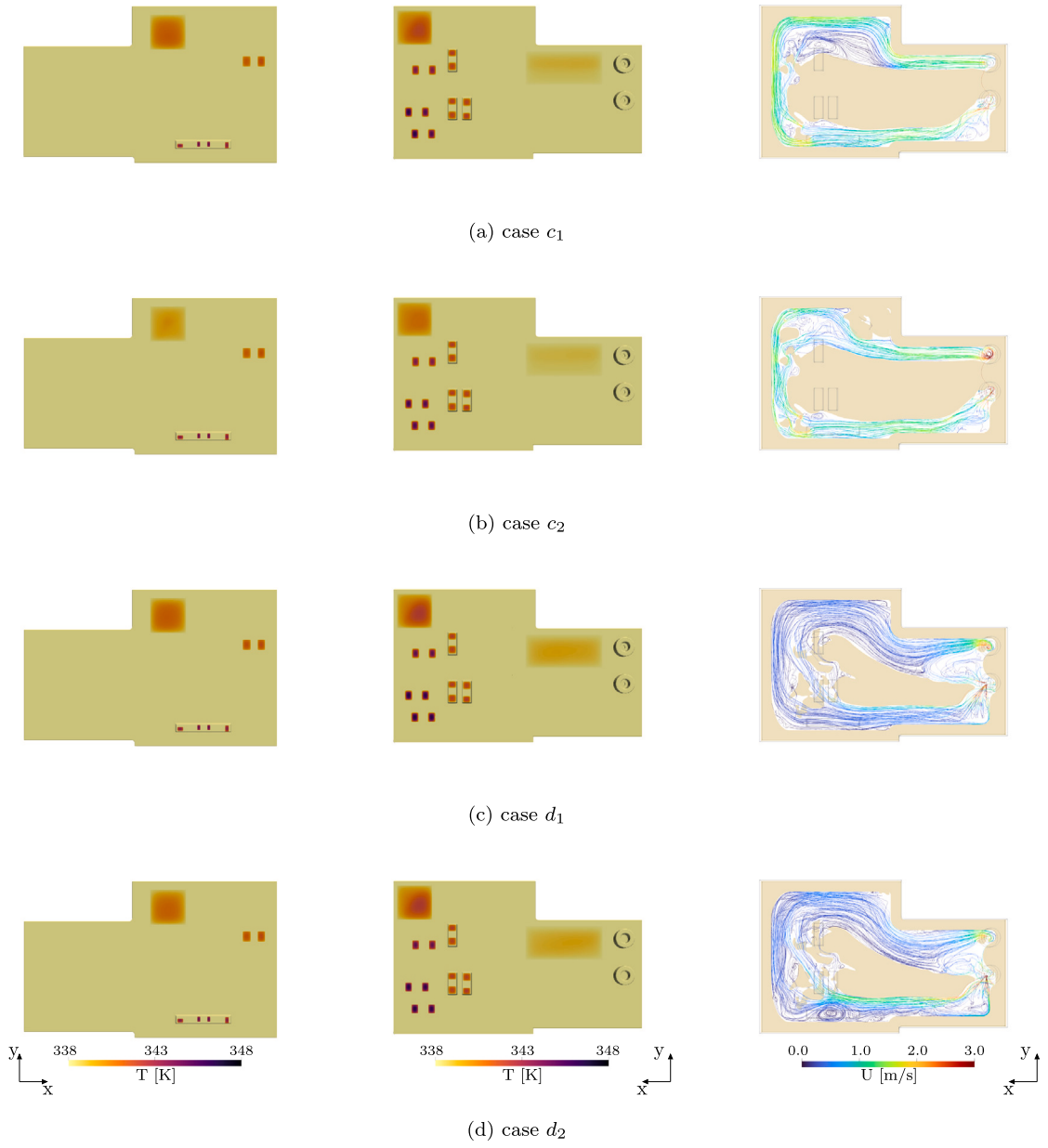


**Fig. 11.** Simulation results for cases $c_1$, $c_2$, $d_1$, and $d_2$: temperature profile of the upper wall (left) and of the bottom wall (center). Velocity streamlines are color-coded to represent the velocity magnitude (right).

interfaces might lead to an underestimation of dissipated power during optimization. Given that dissipated power guides optimal configuration choices, precise verification of solutions is crucial.

Regarding configuration $d$, the variations of $J_1$ and $J_2$ for $d_1$ and $d_2$ are depicted in Fig. 13. For $d_1$, there is a 4% reduction in $J_1$ and a 30% reduction in $J_2$, indicating optimization of both objectives. Conversely, in $d_2$, thermal performance improves slightly by $-33\%$, but dissipated mechanical power increases by 147%. The key distinction between $d_1$ and $d_2$ is the presence of element B. This aligns with the observation in Section 4.1, where solid corresponding to element B introduces power losses throughout the inlet, contributing to the increase in $J_1$. Given the thermal and mechanical performance trade-off, selecting $d_1$ over $d_2$ is the natural choice. Notably, the porous results discussed in Section 4.1 predict a less favorable thermal performance for case $c$ compared to case $d$, yet this disparity is not corroborated in this discussion.

Fig. 7 highlighted how the decrease in $J_2$ was facilitated by redirecting outgoing flux toward heat sources. A similar analysis is performed for case $d_1$, as shown in Fig. 14, indicating that the majority of flow directly reaches the outlet while circulation toward the inlet is significantly dampened. This secondary effect is largely suppressed, strongly influencing the objective functions.

In summary, the characteristics of the topology optimization solution might not persist when solid materials replace the porous distribution. Generally speaking, the topology optimization outcomes tend to be higher than those of the geometries discussed in this section. This discrepancy arises due to several reasons, such as the interpolation of material properties with RAMP and the geometry alteration due to the post-processing to achieve a configuration potentially realizable in practical applications. However, insights gained from the porous material's flow path and temperature distribution can inspire innovative solutions for the optimization problem. Comparing cases $c_1 - c_2$ and $d_1 - d_2$ in Fig. 13, the introduction of secondary elements reduces skin temperature but leads to substantial mechanical power increase. These secondary elements tend to increase around solid material near heat sources, aiding thermal power extraction. A similar thermal effect with less impact on dissipated power could potentially be achieved using pin

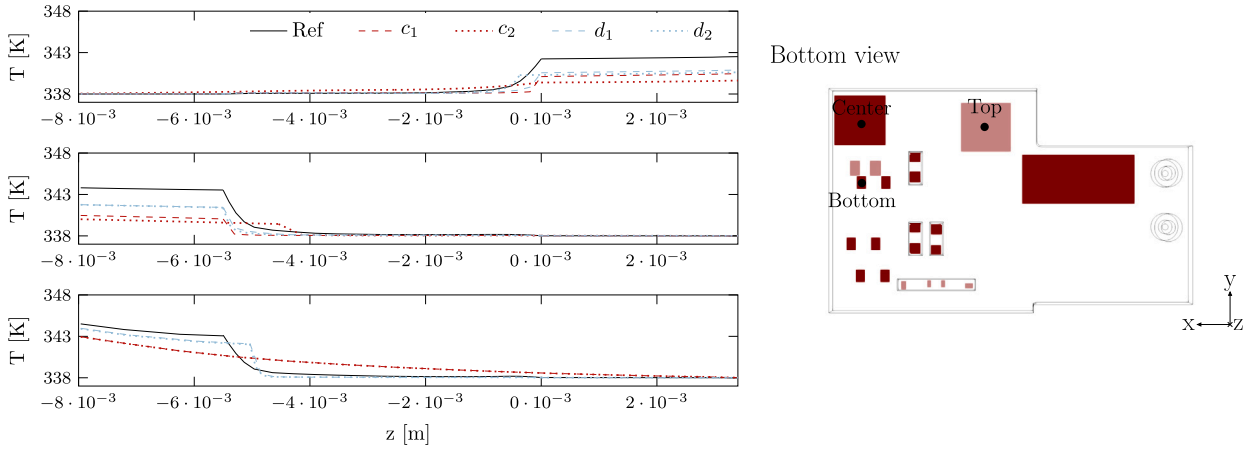


**Fig. 12.** Temperature profiles along the $z$-axis for the reference cases, $c_1$, $c_2$, $d_1$, and $d_2$ at three distinct positions indicated on the map (right figure). Vertical axes correspond respectively to the center of the 35 W heat source (top figure), the 55 W heat source (center figure), and the 22 W heat source (bottom figure).

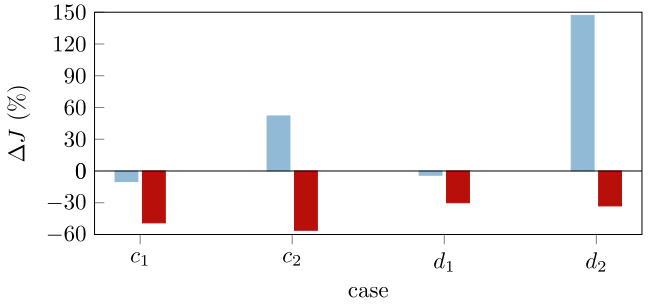


**Fig. 13.** Comparison of the objective functions change for cases $c_1$, $c_2$, $d_1$, and $d_2$ in relation to the starting non-optimized situation, by the monitored quantities $\Delta J_1$ (■) and $\Delta J_2$ (■).

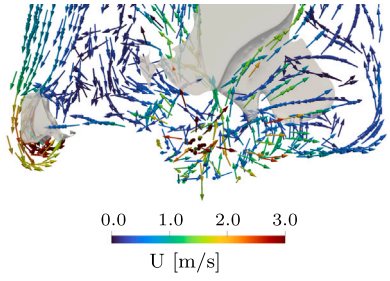


**Fig. 14.** Flow path at the front of the cooling duct for case $d_1$: unlike the situation in case $d$ from Fig. 7, the flow exiting the system in case $d_1$ is not redirected back toward the inlet region.

structures. Additionally, fin-like deflectors could redirect flow toward the inlet region, resembling the solution seen in case $d$ in Fig. 6 and potentially reducing $J_2$.

## 5. Conclusion

We introduced a methodology for Topology Optimization aimed at fluid regions in Couple Fluid–Thermal (CHT) problems. Our approach builds on the principles outlined in [28], incorporating substantial improvements to address multi-region scenarios. Importantly, we extended the original code to accommodate challenges involving multiple regions.

Applying the proposed optimization strategy to a case of industrial interest, a cooling plate for electric motors, allowed us to explore its potential and limits. Changing the relative weights of the multi-objective cost function, we obtained different optimal solutions in which the solid shape varies to favor to decrease of dissipated power or heat sources temperature. Notably, the optimized solution leads to complex alterations in the flow path, resulting in improved performance. We have provided an in-depth exploration of the physical interpretation of these modifications.

The optimal process proposes a porosity distribution that is difficult to manufacture due to the complexity of its surface. We post-processed the result to smooth and realizable surfaces and evaluated the impact of this process on the performance. We highlighted as, despite some characteristic features of the optimal distribution that may not persist when the postprocessing is performed, topology optimization suggests innovative and efficient solutions. The conversion from a porosity distribution to a final, manufacturable, solid component, clearly impacts the performance and strongly depends on final user choices. Being this phase of the design process unavoidable, it should be carefully planned considering the technologies available and imposed constraints.

In conclusion, our discussion underscores that Topology Optimization can effectively tackle multi-objective optimization challenges within CHT systems, even when dealing with industrially significant scenarios. However, owing to the inherent approximations, careful solution verification is imperative during the design phase of optimal components. Nevertheless, given the originality and efficiency of the optimized solutions obtained, we believe that this methodology can offer substantial benefits to designers.

Looking ahead, a logical extension of this work involves the practical implementation of a system inspired by the Topology Optimization solution. This would be followed by experimental validation of the results obtained, bridging the gap between simulation and real-world application.

## Declaration of competing interest

The authors declare that they have no known competing financial interests or personal relationships that could have appeared to influence the work reported in this paper.

## Data availability

Data will be made available on request.

## Acknowledgements

Open Access Funding provided by Politecnico di Milano within the CARE-CRUI Agreement.

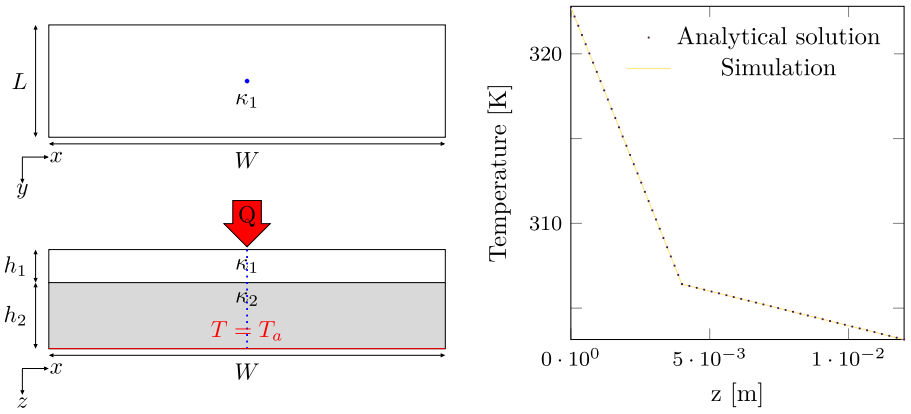


**Fig. 15.** Geometry of the test case utilized for software validation (left) and comparison between the numerical result and the analytical solution (right). The close match between the numerical and analytical solutions provides strong evidence for the correct implementation of the interface boundary condition.

**Table 1**
Geometrical and physical parameters for the validation test case.

| $L$ [m] | $W$ [m] | $h_1$ [m] | $h_2$ [m] | $k_1$ [W m$^{-1}$ K$^{-1}$] | $k_2$ [W m$^{-1}$ K$^{-1}$] | $Q$ [W] | $T_a$ |
|---|---|---|---|---|---|---|---|
| $7 \cdot 10^{-2}$ | $1.4 \cdot 10^{-1}$ | $4 \cdot 10^{-3}$ | $8 \cdot 10^{-3}$ | 5 | 50 | 200 | 303.15 |

## Appendix A. Validation of boundary conditions implementation

In this section, we detail the configuration used to validate our CHT analysis code. We concentrate our analysis on the newly developed components. Specifically, our focus lies on the fixed heat flux and interface boundary conditions.

The geometry of the validation test case is depicted in Fig. 15. This scenario involves heat diffusion within a multi-layer solid structure. The two layers possess rectangular horizontal sections of L × W dimensions, while their thicknesses, represented by $t_1$ and $t_2$, vary. Additionally, their thermal conductivities, $\kappa_1$ and $\kappa_2$, differ. As summarized in Table 1, the upper layer is slimmer and less conductive. The upper surface imparts a uniform heat flux $Q$, whereas the lower wall maintains a fixed temperature $T_a$. For such problems, an analytical solution relying on a Fourier-based temperature representation exists [5], providing a benchmark against which our numerical results can be assessed.

In our comparison, we extracted the temperature along a vertical line passing through the geometry's center (indicated by the dashed blue line in Fig. 15). The numerical and analytical temperature profiles are depicted in the right segment of Fig. 15. Strikingly, the two sets of profiles are nearly indistinguishable, thereby confirming the accurate implementation of the boundary conditions

## Appendix B. On the locality of the solution

The present work employs a gradient-based method to iteratively approach optima. However, this approach often grapples with convergence challenges as solutions tend to converge to local minima rather than the global minimum. To investigate the potential occurrence of such local convergence behavior in our approach, we conducted a re-optimization experiment with an alternative initial condition. Specifically, we initiated the test with $w_1 = 1 \cdot 10^2$ and $w_2 = 1 \cdot 10^{10}$, corresponding to case $d$ in Fig. 6. The optimum solution labeled $c$ from the same figure was used as the initial solution.

Fig. 16 presents the resulting material distribution after 40 optimization cycles. Notably, this solution lies midway between solutions $c$ and $d$. The material configuration within the plate is reminiscent of solution $c$, while the presence of solid material constrains the inlet similarly to solution $f$. The achieved performance aligns with the material distribution: comparable to solution $f$, the accumulation of solid material at the inlet leads to a substantial increase in dissipated

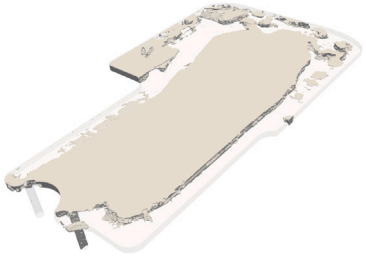

**Fig. 16.** Optimal material distribution attained after 40 iterations, with $w_1 = 1 \cdot 10^2$ and $w_2 = 1 \cdot 10^{10}$, initializing from case $c$ of Fig. 6. Variations from solution $f$ of Fig. 6 highlight the localized nature of the solutions obtained using our current approach.

mechanical power ($\Delta J_1 = +822\%$). Conversely, the thermal performance demonstrates a modest improvement compared to solution $c$, with $\Delta J_2 = -70\%$. These findings underscore that different initial conditions yield diverse material distributions, despite similarities in flow features and optimal values. The challenge of local minima in gradient-based optimization is well-documented [39], and our approach is no exception. While globally-convergent methods [40] can mitigate this issue, their discussion falls beyond the scope of this study.

## References

[1] Fedorov AG, Viskanta R. Three-dimensional conjugate heat transfer in the microchannel heat sink for electronic packaging. Int J Heat Mass Transfer 2000;43(3):399–415. http://dx.doi.org/10.1016/S0017-9310(99)00151-9.

[2] He L, Oldfield MLG. Unsteady Conjugate Heat Transfer Modeling. J Turbomach 2010;133(3). http://dx.doi.org/10.1115/1.4001245.

[3] Kolios MC, Sherar MD, Hunt JW. Large blood vessel cooling in heated tissues: A numerical study. Phys Med Biol 1995;40(4):477. http://dx.doi.org/10.1088/0031-9155/40/4/001.

[4] John B, Senthilkumar P, Sadasivan S. Applied and Theoretical Aspects of Conjugate Heat Transfer Analysis: A Review. Arch Comput Methods Eng 2019;26(2):475–89. http://dx.doi.org/10.1007/s11831-018-9252-9.

[5] Ghioldi F, Hélie J, Piscaglia F. A fast computational method for the optimal thermal design of anisotropic multilayer structures with discrete heat sources for electrified propulsion systems. Int J Heat Mass Transfer 2022;183:122114. http://dx.doi.org/10.1016/j.ijheatmasstransfer.2021.122114.

[6] Dbouk T. A review about the engineering design of optimal heat transfer systems using topology optimization. Appl Therm Eng 2017;112:841–54. http://dx.doi.org/10.1016/j.applthermaleng.2016.10.134.

[7] Lefèvre F, Lallemand M. Coupled thermal and hydrodynamic models of flat micro heat pipes for the cooling of multiple electronic components. Int J Heat Mass Transfer 2006;49(7):1375–83. http://dx.doi.org/10.1016/j.ijheatmasstransfer.2005.10.001.

[8] Song C, Kim J, Cho J. The effect of GaN epilayer thickness on the near-junction thermal resistance of GaN-on-diamond devices. Int J Heat Mass Transfer 2020;158:119992. http://dx.doi.org/10.1016/j.ijheatmasstransfer.2020.119992.

[9] Xu X, Liang X, Ren J. Optimization of heat conduction using combinatorial optimization algorithms. Int J Heat Mass Transfer 2007;50(9):1675–82. http://dx.doi.org/10.1016/j.ijheatmasstransfer.2006.10.037.

[10] Gersborg-Hansen A, Bendsøe MP, Sigmund O. Topology optimization of heat conduction problems using the finite volume method. Struct Multidiscip Optim 2006;31(4):251–9. http://dx.doi.org/10.1007/s00158-005-0584-3.

[11] Aly S, Ogot M, Peltz R. Stochastic approach to optimal aerodynamic shape design. J Aircr 1996;33(5):956–61. http://dx.doi.org/10.2514/3.47041.

[12] Zha G-C, Smith D, Schwabacher M, Rasheed K, Gelsey A, Knight D, Haas M. High-Performance Supersonic Missile Inlet Design Using Automated Optimization. J Aircr 1997;34(6):697–705. http://dx.doi.org/10.2514/2.2241.

[13] Luchini P, Bottaro A. Adjoint equations in stability analysis. Annu Rev Fluid Mech 2014;46(1):493–517. http://dx.doi.org/10.1146/annurev-fluid-010313-141253.

[14] Pironneau O. On optimum design in fluid mechanics. J Fluid Mech 1974;64(1):97–110. http://dx.doi.org/10.1017/S0022112074002023.

[15] Giles M, Pierce N. An Introduction to the Adjoint Approach to Design. Flow Turbul Combust 2000;65:393–415. http://dx.doi.org/10.1023/A:1011430410075.

[16] Fleischli B, Mangani L, Del Rio A, Casartelli E. A discrete adjoint method for pressure-based algorithms. Comput & Fluids 2021;227:105037. http://dx.doi.org/10.1016/j.compfluid.2021.105037.

[17] Towara M, Naumann U. A Discrete Adjoint Model for OpenFOAM. Procedia Comput Sci 2013;18:429–38. http://dx.doi.org/10.1016/j.procs.2013.05.206.

[18] Bendsøe MP, Kikuchi N. Generating optimal topologies in structural design using a homogenization method. Comput Methods Appl Mech Engrg 1988;71(2):197–224. http://dx.doi.org/10.1016/0045-7825(88)90086-2.

[19] Bendsøe MP, Sigmund O. Material interpolation schemes in topology optimization. Arch Appl Mech 1999;69(9):635–54. http://dx.doi.org/10.1007/s004190050248.

[20] Stolpe M, Svanberg K. An alternative interpolation scheme for minimum compliance topology optimization. Struct Multidiscip Optim 2001;22(2):116–24. http://dx.doi.org/10.1007/s001580100129.

[21] Svanberg K. The method of moving asymptotes—a new method for structural optimization. Internat J Numer Methods Engrg 1987;24(2):359–73. http://dx.doi.org/10.1002/nme.1620240207.

[22] Borrvall T, Petersson J. Topology optimization of fluids in Stokes flow. Internat J Numer Methods Fluids 2003;41(1):77–107. http://dx.doi.org/10.1002/fld.426.

[23] Dede EM. Multiphysics topology optimization of heat transfer and fluid flow systems. In: Proceedings of the COMSOL conference. 2009.

[24] Yoon GH. Topological design of heat dissipating structure with forced convective heat transfer. J Mech Sci Technol 2010;24(6):1225–33. http://dx.doi.org/10.1007/s12206-010-0328-1.

[25] Othmer C. A continuous adjoint formulation for the computation of topological and surface sensitivities of ducted flows. Internat J Numer Methods Fluids 2008;58(8):861–77. http://dx.doi.org/10.1002/fld.1770.

[26] Marck G, Nemer M, Harion J-L. Topology Optimization of Heat and Mass Transfer Problems: Laminar Flow. Numer Heat Transfer B 2013;63(6):508–39. http://dx.doi.org/10.1080/10407790.2013.772001.

[27] Subramaniam V, Dbouk T, Harion JL. Topology optimization of conjugate heat transfer systems: A competition between heat transfer enhancement and pressure drop reduction. Int J Heat Fluid Flow 2019;75:165–84. http://dx.doi.org/10.1016/j.ijheatfluidflow.2019.01.002.

[28] Gallorini E, Hèlie J, Piscaglia F. An adjoint-based solver with adaptive mesh refinement for efficient design of coupled thermal-fluid systems. Internat J Numer Methods Fluids 2023;95(7):1090–116. http://dx.doi.org/10.1002/fld.5179.

[29] Gkaragkounis KT, Papoutsis-Kiachagias EM, Giannakoglou KC. The continuous adjoint method for shape optimization in Conjugate Heat Transfer problems with turbulent incompressible flows. Appl Therm Eng 2018;140:351–62. http://dx.doi.org/10.1016/j.applthermaleng.2018.05.054.

[30] The OpenFOAM foundation. URL http://www.openfoam.org/dev.php.

[31] ESI OpenCFD OpenFOAM. URL http://www.openfoam.com/.

[32] Caretto LS, Gosman AD, Patankar SV, Spalding DB. Two calculation procedures for steady, three-dimensional flows with recirculation. In: Cabannes H, Temam R, editors. Proceedings of the third international conference on numerical methods in fluid mechanics. Berlin, Heidelberg: Springer Berlin Heidelberg; 1973, p. 60–8. http://dx.doi.org/10.1007/BFb0112677.

[33] Radenac E, Gressier J, Millan P. Methodology of numerical coupling for transient conjugate heat transfer. Comput & Fluids 2014;100:95–107. http://dx.doi.org/10.1016/j.compfluid.2014.05.006.

[34] Cintolesi C, Nilsson H, Petronio A, Armenio V. Numerical simulation of conjugate heat transfer and surface radiative heat transfer using the P1 thermal radiation model: Parametric study in benchmark cases.. Int J Heat Mass Transfer 2017;107:956–71. http://dx.doi.org/10.1016/j.ijheatmasstransfer.2016.11.006.

[35] Quarteroni A, Valli A. Domain decomposition methods for partial differential equations. Oxford University Press; 1999.

[36] Awasthi K, Reddy DS, Khan MK. Performance comparison among the variants of curved serpentine coil. Phys Fluids 2021;33(7):073604. http://dx.doi.org/10.1063/5.0056606.

[37] Sullivan CB, Kaszynski A. PyVista: 3D plotting and mesh analysis through a streamlined interface for the visualization toolkit (VTK). J Open Source Softw 2019;4(37):1450. http://dx.doi.org/10.21105/joss.01450.

[38] Taubin G. Curve and surface smoothing without shrinkage. In: Proceedings of IEEE international conference on computer vision. 1995, p. 852–7. http://dx.doi.org/10.1109/ICCV.1995.466848.

[39] Sigmund O, Petersson J. Numerical instabilities in topology optimization: A survey on procedures dealing with checkerboards, mesh-dependencies and local minima. Struct Optim 1998;16(1):68–75. http://dx.doi.org/10.1007/BF01214002.

[40] Svanberg K. A class of globally convergent optimization methods based on conservative convex separable approximations. SIAM J Optim 2002;12(2):555–73. http://dx.doi.org/10.1137/S1052623499362822.